Title

A Multicompartmental Diffusion Model for Improved Assessment of Whole-Body Diffusion-weighted Imaging Data and Evaluation of Prostate Cancer Bone Metastases.

Journal

Radiology Imaging Cancer, 5(1)

ISSN

2638-616X

Authors

Conlin, Christopher C
Feng, Christine H
Digma, Leonardino A
et al.

Publication Date

2023

DOI

10.1148/rycan.210115

Peer reviewed

Radiology: Imaging Cancer

TECHNICAL DEVELOPMENT

A Multicompartmental Diffusion Model for Improved Assessment of Whole-Body Diffusion-weighted Imaging Data and Evaluation of Prostate Cancer Bone Metastases

Christopher C. Conlin, PhD • Christine H. Feng, MD • Leonardino A. Digma, BA • Ana E. Rodríguez-Soto, PhD • Joshua M. Kuperman, PhD • Rebecca Rakow-Penner, MD, PhD • David S. Karow, MD, PhD • Nathan S. White, PhD • Tyler M. Seibert, MD, PhD • Michael E. Hahn, MD, PhD • Anders M. Dale, PhD**

From the Departments of Radiology (C.C.C., A.E.R.S., J.M.K., R.R.P., D.S.K., T.M.S., M.E.H., A.M.D.), Radiation Medicine and Applied Sciences (C.H.F., L.A.D., T.M.S.), and Neurosciences (A.M.D.), UC San Diego School of Medicine, 9452 Medical Center Dr, 4W 503, La Jolla, CA 92037; Human Longevity, Inc, San Diego, Calif (D.S.K.); CorTechs Labs, Inc, San Diego, Calif (N.S.W.); Department of Bioengineering, UC San Diego Jacobs School of Engineering, La Jolla, Calif (T.M.S.); and Halıcıoğlu Data Science Institute, UC San Diego, La Jolla, Calif (A.M.D.). Received December 9, 2021; revision requested January 26, 2022; revision received October 25; accepted December 27. **Address correspondence to** M.E.H. (email: *mehahn@health.ucsd.edu*).

* M.E.H. and A.M.D. are co–senior authors.

Supported by the Department of Defense Congressionally Directed Medical Research Program (grant DoD W81XWH-17-1-0618), National Institute of Biomedical Imaging and Bioengineering (grant K08 EB026503), Prostate Cancer Foundation, and UC San Diego Center for Precision Radiation Medicine.

See also commentary by Margolis in this issue. Conflicts of interest are listed at the end of this article.

Radiology: Imaging Cancer 2023; 5(1):e210115 • https://doi.org/10.1148/rycan.210115 • Content codes: GU OI MK

Purpose: To develop a multicompartmental signal model for whole-body diffusion-weighted imaging (DWI) and apply it to study the diffusion properties of normal tissue and metastatic prostate cancer bone lesions in vivo.

Materials and Methods: This prospective study (*ClinicalTrials.gov*: NCT03440554) included 139 men with prostate cancer (mean age, 70 years ± 9 [SD]). Multicompartmental models with two to four tissue compartments were fit to DWI data from whole-body scans to determine optimal compartmental diffusion coefficients. Bayesian information criterion (BIC) and model-fitting residuals were calculated to quantify model complexity and goodness of fit. Diffusion coefficients for the optimal model (having lowest BIC) were used to compute compartmental signal-contribution maps. The signal intensity ratio (SIR) of bone lesions to normal-appearing bone was measured on these signal-contribution maps and on conventional DWI scans and compared using paired *t* tests ($\alpha = .05$). Two-sample *t* tests ($\alpha = .05$) were used to compare compartmental signal fractions between lesions and normal-appearing bone.

Results: Lowest BIC was observed from the four-compartment model, with optimal compartmental diffusion coefficients of 0, 1.1×10^{-3}, 2.8×10^{-3}, and $>3.0 \times 10^{-2}$ mm^2/sec. Fitting residuals from this model were significantly lower than from conventional apparent diffusion coefficient mapping ($P < .001$). Bone lesion SIR was significantly higher on signal-contribution maps of model compartments 1 and 2 than on conventional DWI scans ($P < .008$). The fraction of signal from compartments 2, 3, and 4 was also significantly different between metastatic bone lesions and normal-appearing bone tissue ($P \leq .02$).

Conclusion: The four-compartment model best described whole-body diffusion properties. Compartmental signal contributions from this model can be used to examine prostate cancer bone involvement.

Clinical trial registration no. NCT03440554

Supplemental material is available for this article.

Whole-body MRI is increasingly used to assess bone metastases (1). A key component of whole-body MRI protocols (2,3) is diffusion-weighted imaging (DWI), a functional imaging approach that measures the microscopic diffusion properties of water to probe tissue microstructure (4). Metastatic bone lesions are typically hyperintense on DW images and can be further evaluated quantitatively by computing the apparent diffusion coefficient (ADC) (2,5). However, identification of lesions can be difficult because high signal on DW images is also observed from some benign bone findings (2,6). Interpretation of lesion ADC measurements is also challenging because measurements are confounded by commonly co-occurring factors, such as edema, necrosis, and local perfusion changes (7).

To overcome the limitations of conventional DWI, a number of techniques have been developed that leverage multicompartmental modeling of the diffusion-weighted signal (8–11). Restriction spectrum imaging (RSI) models the diffusion-weighted signal as the sum of signal contributions from distinct, superimposed tissue compartments (11–13). Each compartment is characterized by a fixed diffusion coefficient, such that variation in signal between voxels reflects variation in the proportion of each tissue compartment comprising the total diffusion signal. Recent studies showed that multicompartmental RSI modeling outperforms conventional DWI for assessing cancer within specific organs such as prostate (12,14) and breast (15), but it has yet to be applied to whole-body imaging. Before RSI modeling can be applied to evaluate whole-body metastatic

Abbreviations

ADC = apparent diffusion coefficient, BIC = Bayesian information criterion, DWI = diffusion-weighted imaging, PSA = prostate-specific antigen, ROI = region of interest, RSI = restriction spectrum imaging, SIR = signal intensity ratio

Summary

An optimized four-compartment model better characterizes whole-body diffusion than conventional diffusion-weighted imaging methods. It can be applied to whole-body diffusion MRI data to examine metastatic prostate cancer.

Key Points

- A four-compartment diffusion-weighted imaging (DWI) signal model, with diffusion coefficients of 0, 1.1×10^{-3}, 2.8×10^{-3}, and $>3.0 \times 10^{-2}$ mm^2/sec, yielded lower Bayesian information criterion and better fit to whole-body DWI data than other models.
- Metastatic bone lesion conspicuity was significantly higher on signal-contribution maps of model compartments 1 and 2 compared with conventional DWI ($P < .008$ for all comparisons).
- The fraction of signal from model compartments 2, 3, and 4 was significantly different between metastatic bone lesions and normal-appearing bone tissue ($P \leq .02$ for all comparisons).

Keywords

Whole-Body MRI, Diffusion-weighted Imaging, Restriction Spectrum Imaging, Diffusion Signal Model, Bone Metastases, Prostate Cancer

disease, model parameters need to be established that characterize diffusion properties throughout the body.

This study aimed to develop an RSI model suitable for whole-body DWI by optimizing the number of model compartments and associated diffusion coefficient of each compartment. The optimized model was then applied to examine the diffusion signal properties of normal tissue and metastatic bone lesions in vivo.

Materials and Methods

This Health Insurance Portability and Accountability Act–compliant, institutional review board–approved study was part of a single-center prospective whole-body MRI trial (Clinical Trials Registry no. NCT03440554).

Participants

Patients with suspected prostate cancer were recruited between August 2017 and October 2020. Inclusion criteria for this study were the following: age of 18 years or older, Eastern Cooperative Oncology Group performance status 0–3, ability to lie supine for 60 minutes, and ability to hear and follow verbal instructions. Potential participants were excluded if they had contraindications to MRI, weighed 350 lb (157.5 kg) or more, or were unable to complete the full MRI examination. Participants provided written informed consent for whole-body MRI examination, which was performed in addition to any routine clinically indicated standard-of-care imaging.

Whole-Body MRI Acquisition

All MRI scans were performed with a 3-T clinical scanner (Discovery MR750; GE Healthcare). Five stations were imaged for each participant, corresponding to the head and neck, chest, abdomen, pelvis, and thighs. At each station, axial volumes of DW, T2-weighted, and T1-derived fat-water images were acquired with identical scan coverage. Multishell diffusion data were acquired using four b values–0, 500, 1000, and 2000 sec/mm^2–sampled at one, six, six, and 12 unique diffusion-encoding gradient directions, respectively, within a single acquisition (default tensor; repetition time, 4750 msec; echo time, 75 msec; matrix, 80 × 80 resampled to 128 × 128; field of view, 400 mm; number of sections, 46; section thickness, 6 mm; number of signals acquired, one; acquisition time, 5 minutes 45 seconds). The b = 0 sec/mm^2 volumes were acquired using forward and reverse phase encoding to allow for correction of distortion caused by B0 inhomogeneity (16). T2-weighted data were acquired at a higher resolution for anatomic reference, using a single-shot fast spin-echo sequence (repetition time, 1350 msec; echo time, 113 msec; matrix, 384 × 224 resampled to 512 × 512; field of view, 400 mm; number of sections, 46; section thickness, 6 mm). Acquisition details for the fat-water images are listed in Appendix S1.

MRI Data Postprocessing

All postprocessing and analysis of MRI data were performed using custom programs written in MATLAB (MathWorks) version R2017a. Each multishell DWI volume was corrected for distortions due to B0 inhomogeneity, gradient nonlinearity, and eddy currents (11,16). To prevent image noise from biasing DWI parameter estimates (17), the signal intensity of the multishell DWI volumes was corrected to account for the presence of the noise floor (12,18). Isotropic diffusion was assumed, so the directional DWI volumes at each b value were averaged. For comparison against RSI, conventional ADC maps were computed from these DWI data by fitting the signal at b values 0 and 1000 sec/mm^2 to a monoexponential signal-decay model (19).

Volumetric regions of interest (ROIs) were defined on the DW images by a radiation oncologist (C.H.F., 3 years of experience contouring images) using MIM software (MIM Software, version 7.2.6). ROIs were defined on the DWI volume acquired at the b value on which the lesion was best visualized. This was typically the volume acquired at b = 1000 sec/mm^2, but b = 500 sec/mm^2 and b = 2000 sec/mm^2 were also used. ROIs were reviewed for accuracy and adjusted where necessary by a board-certified radiologist (M.E.H., 6 years of contouring experience). Bone-lesion ROIs were defined for 24 participants over 127 identified bone lesions. Lesions were confirmed through radiologic, clinical, laboratory, and histologic evaluation of all available data by a board-certified radiologist (M.E.H.). In addition to these MRI data, standard-of-care clinical imaging for trial participants included radiography, bone scintigraphy, conventional MRI, and PET/CT scans, which were also examined to assist in confirmation of lesions. Bone-lesion ROIs were defined directly on the DW images, but any other available imaging modality (eg, T2-weighted MRI, fat-water MRI, ADC maps) and all applicable clinical data were used as references to aid in the definition of lesion boundaries.

For each lesion ROI, a corresponding control ROI was defined in normal-appearing bone that contained the same number of voxels as the lesion ROI. For most lesions (120 of 127), this was accomplished by reflecting the lesion ROI across midline, then manually reviewing the reflected ROI to ensure its placement in a normal-appearing region of bone contralateral to the lesion location. For three lesions in vertebrae that were located along the midline, control ROIs were manually placed in normal-appearing vertebral bone either superior or inferior to the lesion within the same imaging station. For four lesions in the sternum or ribs that could not be reflected without also containing lesion tissue, control ROIs were manually placed in normal-appearing bone within the same field of view. Control ROIs were inspected to ensure placement in normal-appearing bone. For three participants with systemic disease throughout the skeleton, no control ROIs were defined. ROIs were also defined for five participants without known metastases and low clinical risk of metastatic disease (based on prostate-specific antigen [PSA] level, cancer stage, and other available clinical imaging) to examine the diffusion properties of various normal tissues in addition to metastatic bone lesions. These ROIs were drawn in the pelvic and thigh stations to avoid respiratory motion artifacts, specifically over the bladder (including urine), prostate, testes, and subcutaneous fat.

Multicompartmental RSI Modeling

RSI models the DWI signal as the summation of signal from distinct tissue compartments:

$$S(b) = \sum_{i=1}^{K} C_i e^{-bD_i},$$

where $S(b)$ denotes the noise-corrected DWI signal at a particular b value, K is the number of tissue compartments, C_i is the unitless weighting factor that describes the contribution of a particular compartment to the overall signal, and D_i is the compartmental diffusion coefficient. By convention, the compartments are ordered from lowest to highest D_i, with the first compartment (C_1) typically describing restricted diffusion (12). Depending on the application, other compartments may variously account for hindered diffusion, free diffusion, and/or flow (11,12,15). To determine optimal K and D_i values for whole-body DWI, simultaneous fitting of the model to data from all 139 participants (>235 million voxels) was performed (12), with K ranging from two to four (maximum K is limited by the number of b values used during acquisition). This fitting process varied the D_i values of the model and selected those that minimized the difference between observed and model-predicted DWI signal across all voxels (see White et al [12] for more implementation details and Conlin et al [20] for a formal examination of the estimation theory underpinnings of the RSI fitting approach). Note that this approach aims to determine globally optimal D_i values that produce the best fit across all voxels collectively, rather than attempting to optimize the diffusion coefficients for each voxel. The relative Bayesian information criterion (ΔBIC [12,21]) and model-fitting residual of each model was recorded to evaluate how well they described the whole-body DWI data. Fitting residual was also examined at the voxel level and ROI level within specific tissues to examine how the fit of each model varied between anatomic structures.

For the optimal RSI model (the model with lowest ΔBIC), signal-contribution (C_i) maps were computed for each participant via nonnegative least-squares fitting of the model to the signal-versus–b value curve from each voxel (12). To quantify bone-lesion appearance on signal-contribution maps, a signal intensity ratio (SIR) (previously used to measure lesion conspicuity [7,12]) was calculated for each lesion by dividing the mean signal within the lesion ROI by the mean signal within the corresponding control ROI. SIR was also computed for conventional DW images and ADC maps for comparison. To account for the inverse relationship between tumor cellularity and ADC values, we reported the inverse SIR on ADC maps, such that a decrease in lesion ADC relative to normal tissue (as expected for prostate cancer tumors) will produce an SIR greater than 1. Compartmental signal fractions for the optimal model were computed by normalizing the C value of each compartment by the sum of all C values: $C_i / \sum_{i=1}^{K} C_i$.

Statistical Analysis

Statistical analyses were performed using MATLAB (MathWorks, version R2017a). ΔBIC (12,21) and model-fitting residual were recorded from the fitting of each model to all voxels. Fitting residual was also examined for individual voxels and within the specific tissue ROIs. Fitting residual was computed as the square root of the sum-of-squared difference between observed and model-predicted signal values. Violin plots were used to show the distribution of fitting residuals in each data set, and paired t tests were used to compare the distribution of fitting residuals between different models. Violin plots were also used to examine the distribution of lesion SIR values on conventional DWI and RSI signal-contribution maps. Paired t tests were used to determine if mean lesion SIR on RSI maps was significantly higher than on conventional DW images. Compartmental signal fractions were compared between bone lesions and normal-appearing bone using two-sample t tests. For all t tests, $P < .05$ was considered to indicate a significant difference. For SIR and signal fraction comparisons with $P < .05$, Cohen d was computed to assess the effect size of the observed difference.

Results

Participant Characteristics

A flowchart illustrating participant selection for this study is shown in Figure 1. A total of 139 participants completed whole-body MRI (mean age, 70 years ± 9 [SD]; PSA level, 79.3 ng/mL ± 234.2). Twenty-four of these participants presented with osseous metastatic lesions (mean age, 69 years ± 11; PSA level, 76.2 ng/mL ± 118.8) that could be confidently contoured for lesion-level analysis. Eighteen of these 24 underwent systemic treatment (such as androgen deprivation therapy and/or chemotherapy) prior to their MRI examination. Five participants without any known metastases and low clinical risk of

metastatic disease (based on PSA level, cancer stage, and available imaging) were also included (mean age, 65 years ± 8; PSA level, 4.8 ng/mL ± 3.3) to examine the diffusion properties of various normal tissues in addition to metastatic bone lesions.

Multicompartmental Model Fitting

Figure 2 shows the relative BIC values and fitting residuals from each model's fit to the voxels from all 139 participants. ΔBIC from the optimized RSI models was lower (more favorable) than that obtained from the monoexponential model used for conventional ADC (290 for the monoexponential model vs 206 for the two-compartment RSI model, 49 for the three-compartment RSI model, and 0 for the four-compartment RSI model). Among RSI models, ΔBIC decreased as the number of model compartments increased. Overall, the four-compartment model yielded lowest BIC. Mean fitting residual values (in units of signal intensity) were 8.0 (median, 5.9) for the monoexponential model, 5.2 (median, 3.5) for the two-compartment RSI model, 2.6 (median, 1.8) for the three-compartment RSI model, and 2.0 (median, 1.3) for the four-compartment RSI model. The mean fitting residual from any RSI model was significantly lower than for the monoexponential model ($P < .001$ for each comparison). Fitting residual also decreased significantly with increasing RSI model order, with mean residual from the three-compartment model lower than from the two-compartment model ($P < .001$), and mean residual from the four-compartment model lower than from the three-compartment model ($P < .001$).

This overall trend of decreasing residual with increasing model order is apparent in both the voxelwise residual maps and tissue-specific ROIs (Fig 3). Mean and median fitting residual values for the different tissue ROIs are listed in Table S1. In normal-appearing bone, prostate, and testes, the fitting residual from any of the RSI models was lower than from the conventional monoexponential model ($P < .001$ for all comparisons). In bone lesions and subcutaneous fat, residuals from the two-compartment RSI model were not lower than from the monoexponential model ($P > .99$ for comparisons of both tissues), but residuals from the three- and four-compartment RSI models were ($P < .001$ for all comparisons). In the urine-filled bladder, only the four-compartment RSI model yielded lower residuals than the monoexponential model ($P > .99$ for the two-compartment RSI model, $P > .99$ for the three-compartment model, $P < .001$ for the four-compartment model). In all tissues examined, the fitting residual from the four-compartment RSI model was significantly lower than from any other model ($P < .001$ for all comparisons). Within bone lesions, the mean fitting residual from the four-compartment RSI model was five times lower than from the conventional monoexponential model.

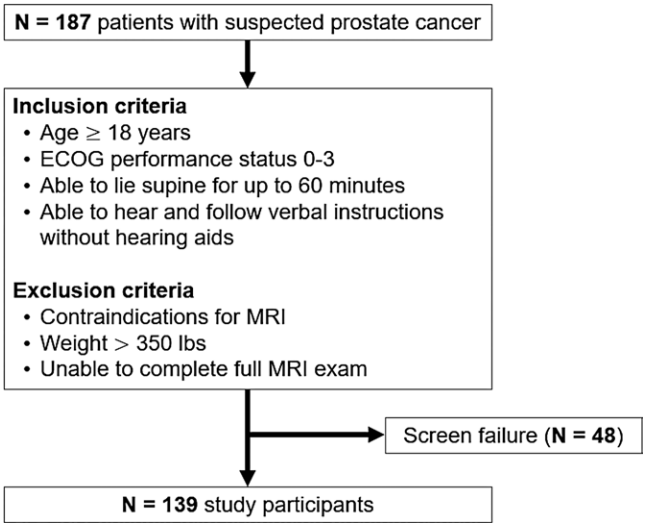

Figure 1: Flowchart illustrates participant selection for this study. ECOG = Eastern Cooperative Oncology Group.

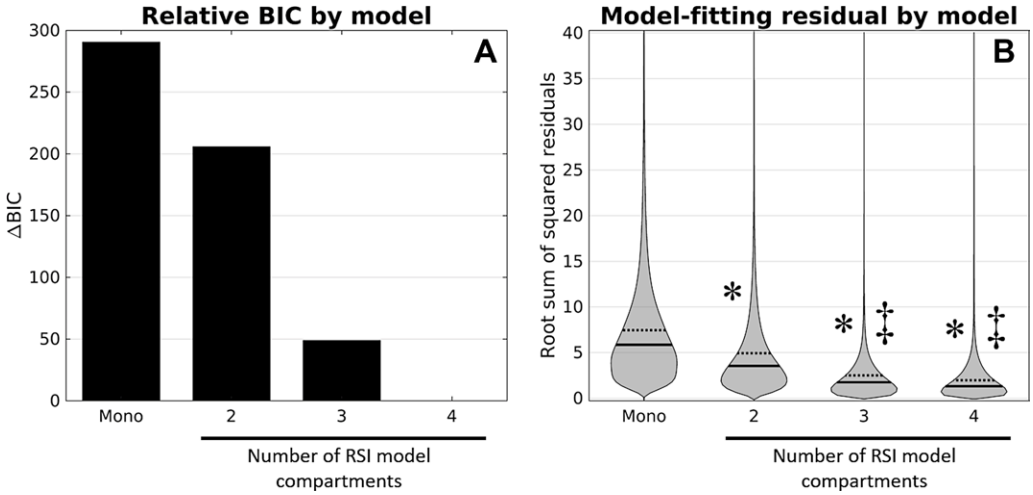

Figure 2: Relative Bayesian information criterion (ΔBIC) and model-fitting residual describe the overall fit of each model to whole-body diffusion data. **(A)** Bars show the ΔBIC value of each model fit to all voxels from all 139 participants. **(B)** Violin plots show the distribution of fitting residuals across all voxels. The median of each distribution is indicated by a solid horizontal line, the mean by a dashed horizontal line. An asterisk (*) indicates that the mean fitting residual for a restriction spectrum imaging (RSI) model is significantly lower ($P < .05$) than for the monoexponential model used for conventional apparent diffusion coefficient mapping (labeled as "Mono"). Double daggers (‡) indicate that the mean fitting residual for an RSI model is significantly lower ($P < .05$) than for the RSI model with one fewer compartment. Lower ΔBIC or residual indicates a better fit to the data.

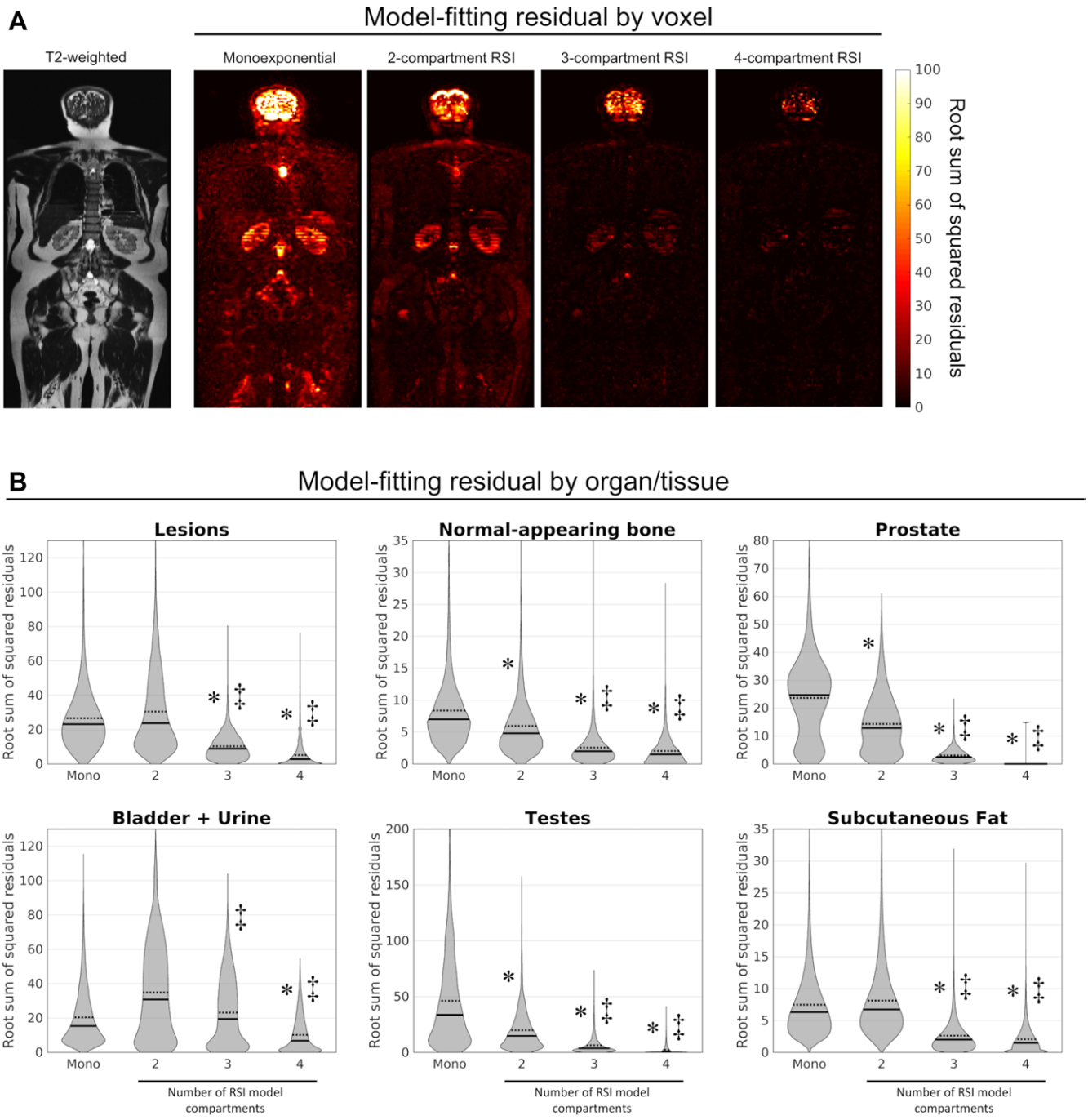

Figure 3: Model-fitting residual at the voxel and ROI level. **(A)** Voxelwise maps of fitting residual in a coronal plane of the same participant (67-year-old man with prostate cancer) using different models. A T2-weighted image of the same plane is included for reference. **(B)** Violin plots show the distribution of fitting residuals for all voxels in each tissue ROI. The median of each distribution is indicated by a solid horizontal line, the mean by a dashed horizontal line. An asterisk (*) indicates that the mean fitting residual for an RSI model is significantly lower ($P < .05$) than for the monoexponential model used for conventional apparent diffusion coefficient mapping (labeled as "Mono"). Double daggers (‡) indicate that the mean fitting residual for an RSI model is significantly lower ($P < .05$) than for the RSI model with one fewer compartment. ROI = region of interest, RSI = restriction spectrum imaging.

Application of the Optimized RSI Model and Examination of Metastatic Bone Lesions

Diffusion coefficients (D_i values) for the optimized four-compartment model were 0, 1.1 × 10^{-3}, 2.8 × 10^{-3}, and >3.0 ×10^{-2} mm^2/sec (D_i values for all models are listed in Table S2). Representative signal-contribution (C_i) maps computed using this model are shown in Figure 4 for a participant with metastatic bone lesions in the sacrum and right femur. The lesions are salient on the C_1 and C_2 maps. Computation time for these voxelwise signal-contribution maps was 3.88 seconds per participant ± 0.37 (0.79 second per station ± 0.02) on a desktop computer with 64-GB RAM and an eight-core, 2.40-GHz CPU (Intel Xeon E5–2630 version 3). Figure 5 compares lesion SIR between C_i maps of the four-compartment RSI model

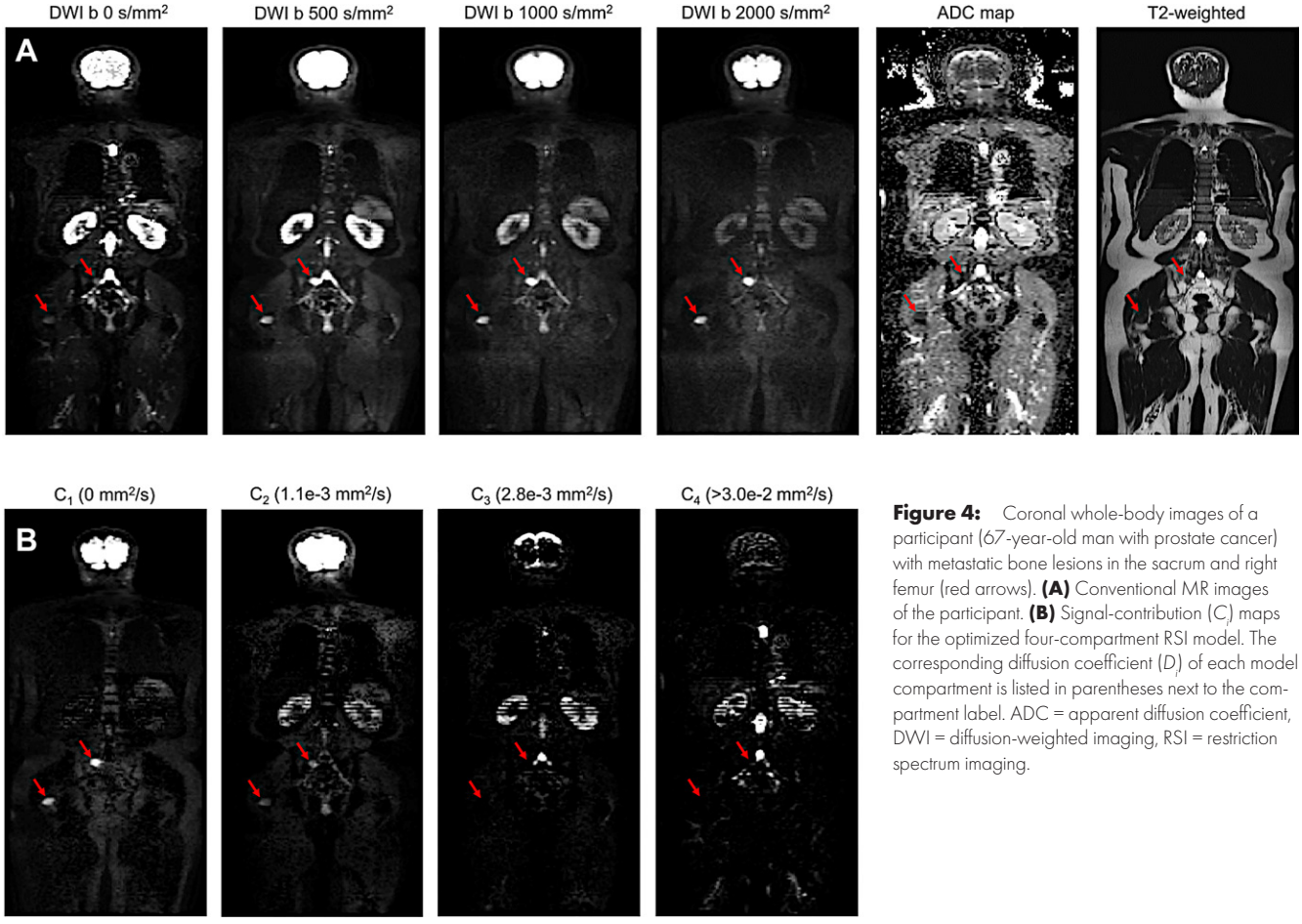

Figure 4: Coronal whole-body images of a participant (67-year-old man with prostate cancer) with metastatic bone lesions in the sacrum and right femur (red arrows). **(A)** Conventional MR images of the participant. **(B)** Signal-contribution (C_i) maps for the optimized four-compartment RSI model. The corresponding diffusion coefficient (D_i) of each model compartment is listed in parentheses next to the compartment label. ADC = apparent diffusion coefficient, DWI = diffusion-weighted imaging, RSI = restriction spectrum imaging.

and conventional DWI. Mean and median SIR values are also listed in Table S3. Lesion SIR was generally highest on RSI C_2 maps, and the overall increase in lesion SIR on C_2 was significant compared with conventional ADC maps ($P < .001$) or DW images ($P < .001$ vs any of the sampled b values). Effect size of the observed increase in SIR on RSI C_2 was $d = 0.7$ (Cohen d) versus ADC, $d = 0.6$ versus b value of 0 sec/mm^2, $d = 0.6$ versus b value of 500 sec/mm^2, $d = 0.6$ versus b value of 1000 sec/mm^2, and $d = 0.7$ versus b value of 2000 sec/mm^2. Lesion SIR was also higher on RSI C_1 maps than on conventional images ($P < .001$ vs conventional ADC map, $P = .008$ vs b value of 0 sec/mm^2, $P = .002$ vs b value of 500 sec/mm^2, $P = .001$ vs b value of 1000 sec/mm^2, $P < .001$ vs b value of 2000 sec/mm^2) but was not as high as on RSI C_2 maps. Effect size of the observed increase in SIR on RSI C_1 was $d = 0.6$ versus ADC, $d = 0.3$ versus b value of 0 sec/mm^2, $d = 0.4$ versus b value of 500 sec/mm^2, $d = 0.4$ versus b value of 1000 sec/mm^2, and $d = 0.4$ versus b value of 2000 sec/mm^2.

Clear differences were observed in compartmental signal fractions between tissues (Fig 6, Table S4). Qualitatively, normal-appearing bone and subcutaneous fat showed the most even distribution of signal from all compartments. Prostate and testes were enriched in signal from compartments 2 and 3. Signal from the urine-filled bladder was almost entirely derived from compartments 3 and 4. Compared with normal-appearing bone, lesions presented with a higher fraction of signal from compartment 2 ($P < .001$) and a lower fraction of signal from compartments 3 ($P = .02$) and 4 ($P < .001$). The effect size of the difference in compartmental signal composition between lesions and normal-appearing bone was $d = 2.4$ for C_2, $d = 0.7$ for C_3, and $d = 1.4$ for C_4.

Discussion

This study extended the RSI modeling approach to whole-body DWI as a first step in the development of biomarkers for prostate cancer bone metastases. Whole-body RSI requires a model that accurately characterizes diffusion, not only in metastatic disease foci, but also normal tissues throughout the body. We leveraged a previously described fitting procedure (12,18) to determine globally optimal whole-body RSI model parameters, using DWI data from whole-body scans of participants with metastatic and nonmetastatic prostate cancer (more than 235 million voxels from 139 participants) for model development. We found that a four-compartment RSI model with D_i values of 0, 1.1×10^{-3}, 2.8×10^{-3}, and $>3.0 \times 10^{-2}$ mm^2/sec yielded lower BIC and better fit to whole-body DWI data than other models under consideration ($P < .001$ for all comparisons).

Improvement in BIC and fit with the four-compartment model was particularly notable in comparison to the monoexponential model used for conventional ADC mapping. The monoexponential model assumes that diffusional displacement

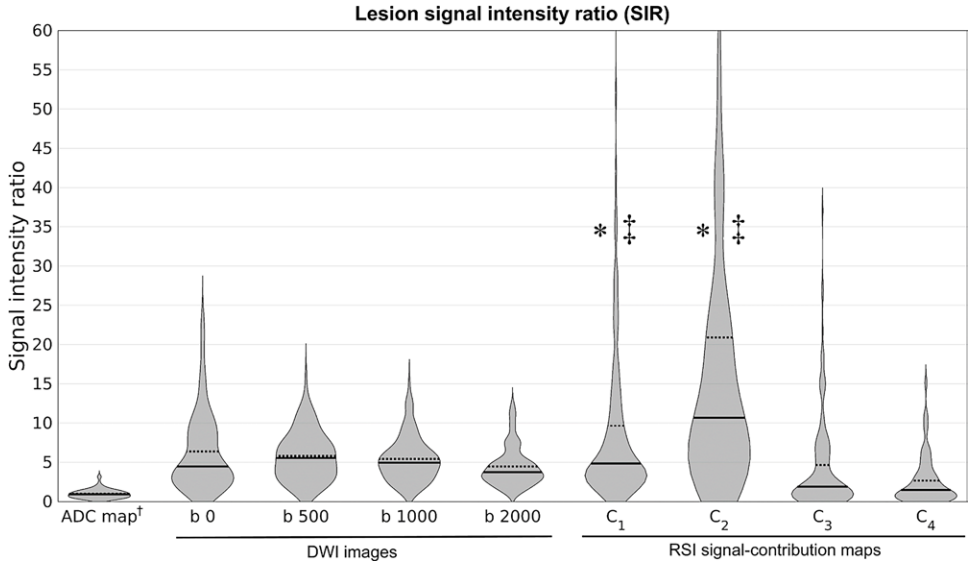

Figure 5: Violin plots show the signal intensity ratio (SIR) distributions of metastatic bone lesions on conventional DW images and compartmental signal-contribution (C_i) maps of the optimized four-compartment RSI model. SIR was calculated for each lesion by dividing the mean signal within the lesion ROI by the mean signal within a control ROI defined on normal-appearing bone. The median of each distribution is indicated by a solid horizontal line, the mean by a dashed horizontal line. An asterisk (*) indicates significantly greater ($P < .05$) mean lesion SIR compared with conventional apparent diffusion coefficient maps. Double daggers (‡) denote significantly greater ($P < .05$) mean lesion SIR compared with DW images at any of the sampled *b* values. The dagger (†) indicates an inverted SIR for ADC maps, such that decreased lesion ADC relative to normal tissue yielded a value > 1. ADC = apparent diffusion coefficient, DWI = diffusion-weighted imaging, ROI = region of interest, RSI = restriction spectrum imaging.

of water within each voxel can be adequately described by a single Gaussian probability distribution, which is generally only true inside fluid-filled structures such as the urinary bladder (22). For most voxels, the complex microstructure of underlying tissue causes the diffusional probability distribution to deviate substantially from the expected Gaussian form and results in a poor fit to the data from the monoexponential model, especially at higher *b* values (22,23). Conversely, multicompartmental RSI models account for different microstructural components co-occurring within a single voxel of tissue and thereby enable a better fit to the data.

Because RSI model D_i values are optimized per compartment, rather than per voxel, computation of RSI signal-contribution maps is a linear estimation problem that can be performed quickly (under 1 second per volume), making it suitable for incorporation into clinical workflows. While the acquisition time for a single RSI volume was nearly 6 minutes, each RSI data set included DWI volumes at four different *b* values and multiple diffusion-encoding gradient directions. Because conventional DW images are directly acquired as part of an RSI protocol, RSI scans may be substituted for conventional DWI acquisitions to offset the additional scan time required for RSI.

Different physiologic aspects encapsulated by the four-compartment model can be appreciated by examining the D_i of each compartment and the anatomic distribution of compartmental signal. An optimal *D* value of 0 mm^2/sec for compartment 1 indicates that diffusion in this compartment is too slow to be reliably measured given the relatively long diffusion times employed during data acquisition (rather than implying a total lack of diffusion). Signal from this compartment is likely attributable to restricted diffusion of intracellular water (11,24), although additional studies are needed for direct histologic correlation. Signal from compartment 1 was enriched in metastatic bone lesions, as demonstrated by their hyperintensity on C_1 signal-contribution maps (that were computed using 0 mm^2/sec as a proxy D_1 value for the precise D_1 that would require shorter diffusion times to measure). High C_1 signal was also observed in the brain, spinal cord, and subcutaneous fat. Compartment 2, with a *D* value of 1.1×10^{-3} mm^2/sec, likely reflects hindered diffusion of water through extracellular extravascular space (11,25). Signal from this compartment was notably hyperintense in bone lesions, brain, viscera, and skeletal muscle. The optimal *D* value of compartment 3 was 2.8×10^{-3} mm^2/sec, similar to the diffusion coefficient of free water (11,26). C_3 signal corresponded to structures composed of or containing a high fraction of fluid, such as the urinary bladder, cerebrospinal fluid, and renal parenchyma. Compartment 4 accounted for rapid pseudodiffusion (intravoxel incoherent motion flow effects [27]), having an optimal *D* much greater than that of free diffusion (>3.0×10^{-2} mm^2/sec). A more precise estimate of the *D* value for compartment 4 would require additional sampling of the DWI signal at *b* values less than 100 sec/mm^2 (28). The smallest nonzero *b* value used for data acquisition in this study (500 sec/mm^2) was too high for reliable measurement of the rapidly decaying signal from vascular flow. Signal from compartment 4 was concentrated in major vessels and highly perfused tissues like the renal cortex, as indicated by their visibility on C_4 signal-contribution maps (computed using an arbitrarily large proxy value for the exact D_4 variable that was not precisely measured in this study).

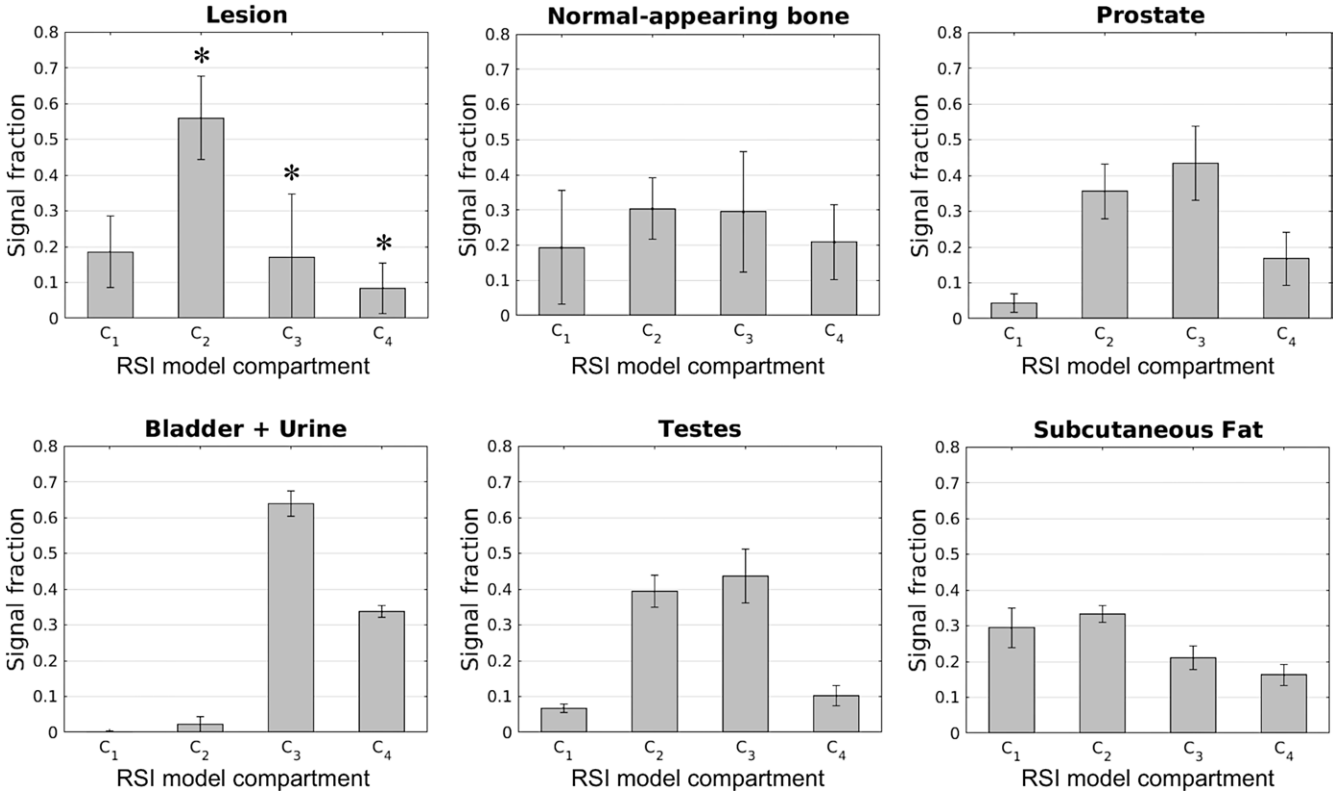

Figure 6: Compartmental signal fractions of different tissues for the optimized four-compartment RSI model. The height of each bar indicates the mean signal fraction across all ROIs, with the overlaid error bar indicating the SD. An asterisk (*) over a bar indicates that the signal fraction in this compartment is significantly different ($P < .05$) in bone lesions compared with normal-appearing bone. ROI = region of interest, RSI = restriction spectrum imaging.

Metastatic bone lesion SIR was significantly higher on RSI C_1 and C_2 signal-contribution maps than conventional DW images or ADC maps. C_2 signal in particular shows the highest SIR of any model compartment and could potentially help distinguish metastatic bone lesions from normal bone. However, we emphasize that the aim of this study was the technical development of a whole-body RSI model, en route to evaluation of its clinical efficacy. Future studies will formally examine whether RSI improves the detection of metastatic bone lesions compared with conventional approaches.

The decomposition of diffusion signal into different microstructural compartments using RSI may also provide some insight into the physiology of prostate cancer bone involvement. The significant increase in C_2 signal fraction observed in metastatic lesions compared with normal bone suggests considerable remodeling of the extracellular matrix (29), while the significant decrease in C_3 and C_4 signal fractions may indicate a concomitant reduction in local free water and perfusion. Given the large proportion of participants in our study who underwent systemic therapy prior to their MRI examination, RSI signal changes may also reflect treatment effects superimposed on cancer-induced physiologic changes. Treatment effects may also explain the lack of any significant difference in fraction of signal from compartment 1 between metastatic lesions and normal-appearing bone. C_1 signal is highly correlated with tissue cellularity (13,30,31), which might be expected to increase as a result of metastatic lesion growth. Cytotoxic chemotherapy or radiation treatments, however, would counteract cancerous hyperplasia (11,32) and perhaps mitigate C_1 signal increase. Furthermore, high cellularity of normal marrow adipose tissue and red bone marrow could mask cancerous hyperplasia on C_1 images even without treatment effects. Subsequent investigations will specifically examine how different histologic aspects of prostate cancer bone involvement affect the signal from different RSI model compartments.

A potential limitation of this study was that our bone-lesion data set was not uniform with respect to treatment; some participants underwent therapy prior to their MRI examination while others were treatment naive. However, because treatment heterogeneity is typical of the broader patient population for which whole-body MRI scans are prescribed, it is not expected to limit the applicability of our findings. Furthermore, the proposed model is meant to describe whole-body diffusion properties generally, not only the properties of prostate cancer bone metastases. The application of the model to evaluate prostate cancer bone metastases was intended as a demonstration of the potential clinical utility of the model, not to imply that it is only suitable for that specific disease phenotype. Because the model was developed using all voxels from many whole-body data sets, of which only a small fraction was from metastatic bone lesions, the treatment status of individual lesions has a negligible impact on the global model parameters determined in this study. Another limitation was that we were unable to reliably compare the RSI signal properties of treated lesions to those of untreated lesions. Because RSI C_1 signal intensity is strongly correlated with cellularity, however, we might

anticipate significantly lower C_1 signal from lesions after cytotoxic chemotherapy or radiation treatments (11,32). This is an area of interest for future study.

In summary, an optimized RSI model may provide a more comprehensive characterization of whole-body diffusion than conventional DWI methods. Higher lesion signal intensity on RSI signal-contribution maps may help to discriminate between cancerous and normal bone during whole-body cancer assessment, although formal clinical efficacy of RSI was not specifically investigated here. Examination of RSI compartmental signal contributions may provide insight into microstructural changes that accompany prostate cancer bone involvement.

Data sharing: Data generated or analyzed during the study are available from the corresponding author by request.

Author contributions: Guarantors of integrity of entire study, **C.C.C., M.E.H., A.M.D.**; study concepts/study design or data acquisition or data analysis/interpretation, all authors; manuscript drafting or manuscript revision for important intellectual content, all authors; approval of final version of submitted manuscript, all authors; agrees to ensure any questions related to the work are appropriately resolved, all authors; literature research**, C.C.C., C.H.F., L.A.D., A.E.R.S., T.M.S., M.E.H., A.M.D.**; clinical studies, **C.C.C., C.H.F., J.M.K., R.R.P., D.S.K., T.M.S., M.E.H., A.M.D.**; statistical analysis**, C.C.C., N.S.W., T.M.S., M.E.H., A.M.D.**; and manuscript editing, **C.C.C., C.H.F., L.A.D., A.E.R.S., R.R.P., N.S.W., T.M.S., M.E.H., A.M.D.**

Disclosures of conflicts of interest: **C.C.C.** Department of Defense Congressionally Directed Medical Research Program, award ID: DoD W81XWH-17-1-0618; Prostate Cancer Foundation Challenge Award. **C.H.F.** No relevant relationships. **L.A.D.** No relevant relationships. **A.E.R.S.** No relevant relationships. **J.M.K.** No relevant relationships. **R.R.P.** GE research grant; NIH research grants (NIH R37CA249659, NIH SBIR R44 CA268468-01, NIH U54HD104393, NIH R01 CA255780); honoraria for lecture from Educational Symposia; scientific advisory board member of Imagine Scientific, Cortechs Labs, and Academy of Radiology; stock options in CureMetrix and Cortechs Labs. **D.S.K.** No relevant relationships. **N.S.W.** Currently employed at Cortechs Labs. **T.M.S.** Grants to institution (NIH/NIBIB #K08EB026503. DoD/CDMRP PC 160673. Prostate Cancer Foundation, University of California); research agreements form GE Healthcare to institution; consulting fees to author from Varian Medical Systems, Cortechs Labs, and Healthlytix; stock options in Cortechs Labs; equipment from GE Healthcare (research agreement with institution). **M.E.H.** Grant support to institution from U.S. Department of Defense, Prostate Cancer Foundation, and GE Healthcare; consulting fees from Healthlytix (consulting on prostate MRI). **A.M.D.** Comprehensive research agreement between GE Healthcare and UCSD; inventor on a patent covering multicompartment diffusion MRI modeling: US-9,404,986 "Measuring Biological Tissue Parameters Using Diffusion Magnetic Resonance Imaging;" founder and equity holder in Cortechs.ai; scientific advisory boards of Cortechs.ai, Human Longevity, and the Mohn Medical Imaging and Visualization Centre in Bergen, Norway.

References

1. Larbi A, Omoumi P, Pasoglou V, et al. Whole-body MRI to assess bone involvement in prostate cancer and multiple myeloma: comparison of the diagnostic accuracies of the T1, short tau inversion recovery (STIR), and high b-values diffusion-weighted imaging (DWI) sequences. Eur Radiol 2019;29(8):4503–4513.
2. Padhani AR, Lecouvet FE, Tunariu N, et al. METastasis Reporting and Data System for Prostate Cancer: Practical Guidelines for Acquisition, Interpretation, and Reporting of Whole-body Magnetic Resonance Imaging-based Evaluations of Multiorgan Involvement in Advanced Prostate Cancer. Eur Urol 2017;71(1):81–92.
3. Arita Y, Takahara T, Yoshida S, et al. Quantitative Assessment of Bone Metastasis in Prostate Cancer Using Synthetic Magnetic Resonance Imaging. Invest Radiol 2019;54(10):638–644.
4. Le Bihan D. Molecular diffusion nuclear magnetic resonance imaging. Magn Reson Q 1991;7(1):1–30.
5. Lecouvet FE, Talbot JN, Messiou C, Bourguet P, Liu Y, de Souza NM; EORTC Imaging Group. Monitoring the response of bone metastases to treatment with Magnetic Resonance Imaging and nuclear medicine techniques: a review and position statement by the European Organisation for Research and Treatment of Cancer imaging group. Eur J Cancer 2014;50(15):2519–2531.
6. Koh D-M, Blackledge M, Padhani AR, et al. Whole-body diffusion-weighted MRI: tips, tricks, and pitfalls. AJR Am J Roentgenol 2012;199(2):252–262.
7. White NS, McDonald CR, Farid N, Kuperman JM, Kesari S, Dale AM. Improved conspicuity and delineation of high-grade primary and metastatic brain tumors using "restriction spectrum imaging": quantitative comparison with high B-value DWI and ADC. AJNR Am J Neuroradiol 2013;34(5):958–964, S1.
8. Panagiotaki E, Chan RW, Dikaios N, et al. Microstructural characterization of normal and malignant human prostate tissue with vascular, extracellular, and restricted diffusion for cytometry in tumours magnetic resonance imaging. Invest Radiol 2015;50(4):218–227.
9. Chatterjee A, Bourne RM, Wang S, et al. Diagnosis of Prostate Cancer with Noninvasive Estimation of Prostate Tissue Composition by Using Hybrid Multidimensional MR Imaging: A Feasibility Study. Radiology 2018;287(3):864–873.
10. Kim D, Doyle EK, Wisnowski JL, Kim JH, Haldar JP. Diffusion-relaxation correlation spectroscopic imaging: A multidimensional approach for probing microstructure. Magn Reson Med 2017;78(6):2236–2249.
11. White NS, McDonald C, Farid N, et al. Diffusion-weighted imaging in cancer: physical foundations and applications of restriction spectrum imaging. Cancer Res 2014;74(17):4638–4652.
12. Conlin CC, Feng CH, Rodriguez-Soto AE, et al. Improved Characterization of Diffusion in Normal and Cancerous Prostate Tissue Through Optimization of Multicompartmental Signal Models. J Magn Reson Imaging 2021;53(2):628–639.
13. Rakow-Penner RA, White NS, Parsons JK, et al. Novel technique for characterizing prostate cancer utilizing MRI restriction spectrum imaging: proof of principle and initial clinical experience with extraprostatic extension. Prostate Cancer Prostatic Dis 2015;18(1):81–85.
14. Feng CH, Conlin CC, Batra K, et al. Voxel-level Classification of Prostate Cancer on Magnetic Resonance Imaging: Improving Accuracy Using Four-Compartment Restriction Spectrum Imaging. J Magn Reson Imaging 2021;54(3):975–984.
15. Andreassen MMS, Rodríguez-Soto AE, Conlin CC, et al. Discrimination of Breast Cancer from Healthy Breast Tissue Using a Three-component Diffusion-weighted MRI Model. Clin Cancer Res 2021;27(4):1094–1104.
16. Holland D, Kuperman JM, Dale AM. Efficient correction of inhomogeneous static magnetic field-induced distortion in Echo Planar Imaging. Neuroimage 2010;50(1):175–183.
17. Taylor PA, Biswal B. Geometric analysis of the b-dependent effects of Rician signal noise on diffusion tensor imaging estimates and determining an optimal b value. Magn Reson Imaging 2011;29(6):777–788.
18. Karunamuni RA, Kuperman J, Seibert TM, et al. Relationship between kurtosis and bi-exponential characterization of high b-value diffusion-weighted imaging: application to prostate cancer. Acta Radiol 2018;59(12):1523–1529.
19. Vidić I, Egnell L, Jerome NP, et al. Modeling the diffusion-weighted imaging signal for breast lesions in the b = 200 to 3000 s/mm2 range: quality of fit and classification accuracy for different representations. Magn Reson Med 2020;84(2):1011–1023.
20. Conlin CC, Seibert TM, Dale AM. Optimal protocol design for diffusion-weighted imaging of the prostate: an estimation theory examination of parameter estimate variance. medRxiv 2022;2022.02.26.22271561. Posted February 28, 2022. Accessed October 2022.
21. Schwarz G. Estimating the Dimension of a Model. Ann Stat 1978;6(2):461–464.
22. Jensen JH, Helpern JA, Ramani A, Lu H, Kaczynski K. Diffusional kurtosis imaging: the quantification of non-gaussian water diffusion by means of magnetic resonance imaging. Magn Reson Med 2005;53(6):1432–1440.
23. Kärger J. NMR self-diffusion studies in heterogeneous systems. Adv Colloid Interface Sci 1985;23:129–148.
24. Hope TR, White NS, Kuperman J, et al. Demonstration of Non-Gaussian Restricted Diffusion in Tumor Cells Using Diffusion Time-Dependent Diffusion-Weighted Magnetic Resonance Imaging Contrast. Front Oncol 2016;6:179.
25. Koh TS, Bisdas S, Koh DM, Thng CH. Fundamentals of tracer kinetics for dynamic contrast-enhanced MRI. J Magn Reson Imaging 2011;34(6):1262–1276.
26. Le Bihan D. Looking into the functional architecture of the brain with diffusion MRI. Nat Rev Neurosci 2003;4(6):469–480.
27. Le Bihan D, Breton E, Lallemand D, Aubin ML, Vignaud J, Laval-Jeantet M. Separation of diffusion and perfusion in intravoxel incoherent motion MR imaging. Radiology 1988;168(2):497–505.

28. Döpfert J, Lemke A, Weidner A, Schad LR. Investigation of prostate cancer using diffusion-weighted intravoxel incoherent motion imaging. Magn Reson Imaging 2011;29(8):1053–1058.
29. Kolb AD, Bussard KM. The Bone Extracellular Matrix as an Ideal Milieu for Cancer Cell Metastases. Cancers (Basel) 2019;11(7):1020.
30. Liss MA, White NS, Parsons JK, et al. MRI-Derived Restriction Spectrum Imaging Cellularity Index is Associated with High Grade Prostate Cancer on Radical Prostatectomy Specimens. Front Oncol 2015;5:30.
31. McCammack KC, Schenker-Ahmed NM, White NS, et al. Restriction spectrum imaging improves MRI-based prostate cancer detection. Abdom Radiol (NY) 2016;41(5):946–953.
32. Padhani AR, Gogbashian A. Bony metastases: assessing response to therapy with whole-body diffusion MRI. Cancer Imaging 2011;11 Spec No A(1A):S129–S145.